J. Fluid Mech. (1992), *vol.* 244, *pp.* 101–129

Numerical simulation of low-Reynolds-number turbulent flow through a straight square duct

By S. GAVRILAKIS

IMHEF–DME, Ecole Polytechnique Fédérale de Lausanne, Switzerland 1015

(Received 14 June 1991 and in revised form 15 April 1992)

The mean flow and turbulent statistics obtained from the numerical simulation of the fully developed turbulent flow through a straight duct of square cross-section are reported. The Reynolds number based on the bulk velocity and hydraulic diameter is 4410. Spatial and temporal approximations of the equations of motion were derived from standard finite-difference techniques. To achieve sufficient spatial resolution 16.1×10^6 grid nodes were employed. Turbulent statistics along the wall bisectors show good agreement with plane channel data despite the influence of the sidewalls in the former flow. The mean secondary flow field consists of two counter-rotating cells symmetrically placed about the corner bisectors with their common flow towards each corner with strong evidence for the existence of a smaller and much weaker pair situated about the wall bisectors. The mean streamwise vorticity of each corner cell is found to be associated with a stronger vorticity distribution of the opposite sign having an absolute maximum on the nearest duct wall.

1. Introduction

The turbulent flow field in the vicinity of a smooth corner is subjected to a remarkable structural change that results in, for most values of the angle, a mean velocity field in planes perpendicular to its boundaries. Prompted by the measurements in ducts of rectangular and triangular cross-section of Nikuradse (see Schlichting 1979, p. 612), Prandtl was first to recognize the distinct origins of such flows which are now commonly referred to as secondary flows of Prandtl's second kind. Secondary flows of Prandtl's first kind arise from the skewing of the mean cross-stream vorticity and the associated secondary velocities are generally much stronger than those induced by turbulence (Bradshaw 1987).

Complete information on such flows is believed to be available, in principle, from the full Navier–Stokes equations together with the appropriate boundary conditions. The Reynolds-averaged form of these equations has been used to highlight aspects of the secondary flows of the second kind as well as to guide experimental and modelling work (for a review see Demuren & Rodi 1984). The appearance of unknown correlations in the ensemble-averaged equations limits their usefulness as a source of information although they may serve as a check on the consistency of models. Some of this information is, however, accessible through direct numerical simulation. The present paper reports on the results of a simulation of the fully developed turbulent flow through a straight duct of square cross-section at a low Reynolds number. Although duct flows are common in practice, the effects of the corners on the turbulence is of wider practical interest.

The difference in the Reynolds number between the simulated flow and most experiments (see Demuren & Rodi 1984) is quite large, one order of magnitude or more, but it appears likely that the mechanisms driving the corner secondary flows at disparate Reynolds numbers are similar. The present results (§6 below) also show that the terms of the equation for the mean streamwise vorticity attain their largest values in regions where viscous effects on turbulence are significant; an associated result concerning the importance of anisotropy in the viscous dissipation rate was published by Speziale (1986). The existence of such regions is assured for all laboratory Reynolds numbers. However, in plane channel flows at low Reynolds numbers, the influence of one wall has been found to extend to the vicinity of the other (Wei & Willmarth 1989; Teitel & Antonia 1990). For square duct flows, this influence would be modified by the events that make up the secondary flows – which are themselves an example of the opposite wall interaction – and are present at higher turbulent Reynolds numbers.

A detailed description of the nature of the secondary flows in corners would require understanding the turbulent field that causes them. As a first step towards this goal, a number of turbulence statistics in a square duct are documented below, which also reveal the importance of the flow field in the vicinity of the walls close to each corner – an area previously overlooked. The simulation results are compared with experimental data and spectral simulation results from plane channel flows. The numerical method used in the simulation is described in §2. The different constraints on the choice of the Reynolds number are described in §3 together with the coarse grid tests that were necessary since experimental data at low Reynolds numbers are scarce. The mean velocity field is three-dimensional with the streamwise component being dominant. The simulation results are presented in §4. Comparisons with plane channel flows in §5 are made with data from the duct wall bisectors only. Additional comparisons with recent measurements in square ducts at low Reynolds number are also made. The computed terms of the equation for the mean streamwise vorticity are presented in §6, followed by the concluding §7.

2. Numerical method

In an Eulerian frame of reference, the mathematical form of the force–momentum balance for a constant-property incompressible Newtonian fluid at a point in space is given by the Navier–Stokes equation:

$$\frac{\partial u_i}{\partial t}+\frac{\partial u_i u_j}{\partial x_j} = -\frac{\partial p}{\partial x_i}+\nu\frac{\partial^2 u_i}{\partial x_j \partial x_j}+F_i, \quad i = 1,2,3, \tag{1}$$

and the continuity equation,

$$\frac{\partial u_j}{\partial x_j} = 0, \tag{2}$$

where the summation convention applies over the repeated subscripts, p is the kinematic pressure, ν the kinematic viscosity and F_i represents an external force term. For the present computational study it is assumed that the fluid fills a rectangular domain bounded by four plain solid walls arranged in two parallel pairs, and two flow-through sides as shown in figure 1 (a). In the direction normal to the two open boundaries the mean flow is non-zero and it is designated the streamwise direction x. The direction parallel to the y-axis will be referred to as the normal direction and that parallel to the z as the spanwise direction. The origin of the axes system is at point A. The two wall bisectors divide the duct cross-section into four quadrants; the one closest to the axes origin will be referred to as the first quadrant.

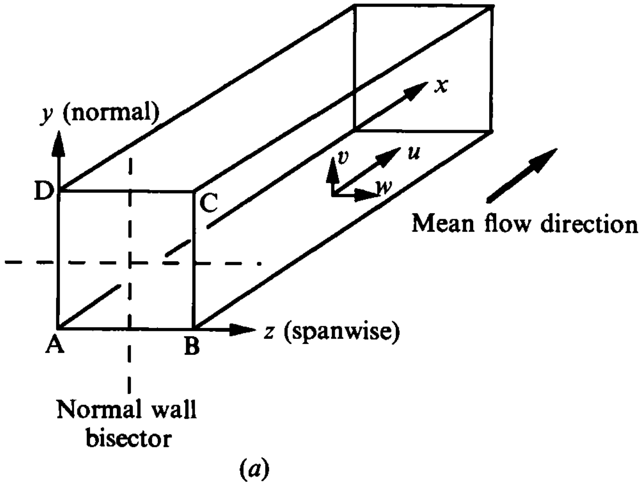

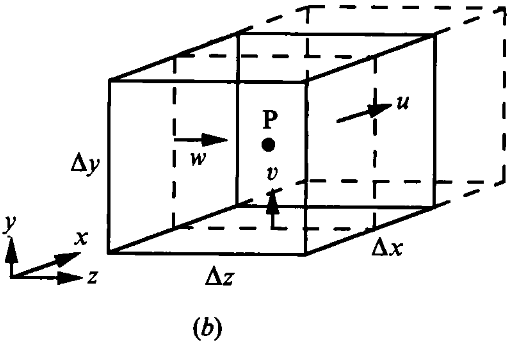

FIGURE 1. (*a*) Axes system, geometry and notation for the square duct flow. (*b*) Finite-difference cell showing the positions where the flow variables are defined.

Other definitions are given on figure 1(*a*). To avoid having to specify inflow and outflow conditions at the open boundaries, it is also assumed that the instantaneous flow field is periodic along the streamwise direction. This artifice is compatible with the fully developed duct flow provided that the streamwise extent of the computational domain is sufficient to ensure the spatial decorrelation of the turbulent statistics within it. The F_t term is taken as the mean part of the pressure gradient field which is used to drive the flow by setting its streamwise component to a non-zero constant.

The spatial approximation of (1) and (2) is obtained by a second-order finite-difference method applied to the staggered grid arrangement shown on figure 1(*b*). Equations for the grid-averaged velocity components are obtained by integrating each momentum equation over a grid volume surrounding the point on which each velocity component is defined. The continuity equation is averaged over the grid volume surrounding the pressure node. The technique is essentially that of Schumann (1975) and it is therefore not reproduced here. It differs from Schumann's in that the present implementation can accommodate non-uniform grids in both cross-stream (y, z) directions, and in that the subgrid terms are neglected.

The formal accuracy of spatial discretization is second order for uniformly distributed grid points. This convergence rate is maintained for non-uniform grids when the rate of change of grid spacing along each direction is sufficiently smooth, albeit with an increase in the absolute value of the truncation error. This has been confirmed by computing the laminar flow profile through a straight square duct for which the analytical solution is known. For the computations reported below, the changes in the size of neighbouring grids is always below 6%, which is found to be well within the radius for second-order convergence. The error terms due to the various finite-difference approximations were estimated using Taylor series expansions. The leading terms modifying the equations of motion were found to involve higher-order mixed derivatives with grid-dependent numerical factors not exceeding 6% of the molecular viscosity.

The discrete form of the advection terms in the momentum equations conserve total momentum. In addition, global conservation of the variance of each velocity component is also maintained provided that the discrete form of the continuity equation about the pressure node is obeyed exactly. In the present calculations, the residual in the discrete continuity equation scaled with the mean friction velocity and length of the duct side is less than 10^{-11}.

The time advancement scheme is similar to the Kim & Moin (1985) adaptation of Chorin's fractional step method, which allows the implicit treatment of the viscous diffusion terms. Defining

$$G_i^n = \left[-\frac{\delta u_i u_j}{\delta x_j} + \nu \frac{\delta^2 u_i}{\delta x^2}\right]^n,$$

where δ is the finite-difference operator, with the superscript n denoting the discrete time level, then, using $\hat{}$ to denote the intermediate values of the velocity, the field variables at step $n+1$ are found by

$$\frac{\hat{u}_i - u_i^n}{\Delta t} = \tfrac{3}{2}G_i^n - \tfrac{1}{2}G_i^{n-1} + \frac{\nu}{2}\left[\frac{\delta^2}{\delta y^2} + \frac{\delta^2}{\delta z^2}\right](\hat{u}_i + u_i^n) + F_i, \tag{3}$$

$$\frac{u_i^{n+1} - \hat{u}_i}{\Delta t} = -\frac{\delta \phi^{n+\frac{1}{2}}}{\delta x_i} \tag{4}$$

and

$$\frac{\delta u_j^{n+1}}{\delta x_j} = 0. \tag{5}$$

The auxiliary potential ϕ is related to the pressure by

$$p = \phi - \frac{\nu \Delta t}{2}\left[\frac{\delta^2}{\delta y^2} + \frac{\delta^2}{\delta z^2}\right]\phi \tag{6}$$

and is defined on the same nodes as p.

The streamwise diffusion terms have been treated explicitly because their contribution to the time-step stability limit is at least two orders of magnitude above that due to the inertial terms.

The solution of (3) for the provisional velocity requires the inversion of one pentadiagonal matrix for each discrete x-station. This can be avoided by using the following approximate factorization:

$$\left(1 - \beta\frac{\delta^2}{\delta y^2} - \beta\frac{\delta^2}{\delta z^2}\right)(\hat{u}_i - u_i^n) \approx \left(1 - \beta\frac{\delta^2}{\delta y^2}\right)\left(1 - \beta\frac{\delta^2}{\delta z^2}\right)(\hat{u}_i - u_i^n), \tag{7}$$

where $\beta = \frac{1}{2}\nu\Delta t$. This reduces the problem to the inversion of two tridiagonal matrices. The error term introduced in (7) is of the same order as the time truncation of the Crank–Nicholson or Adams–Bashforth schemes. The matrices arising in (7) involve unknown boundary values of $\hat{u}_i$. These are found by applying (4) to the boundaries and using Taylor's expansion in the time variable for approximating the gradient of ϕ to that of the previous time level, thus:

$$\hat{u}_i = u_i^{n+1} + \Delta t \frac{\partial \phi^{n-\frac{1}{2}}}{\partial x_i} + O(\Delta t^2).$$

This procedure has been found to be stable.

The provisional velocity $\hat{u}_i$ does not obey continuity. This constraint is implicitly enforced by a suitable choice of ϕ with subsequent application of (4). An equation for ϕ is derived by taking the divergence of (4) and applying the continuity (5) for the velocity at the next time level, this results in

$$\frac{\delta^2 \phi^{n+\frac{1}{2}}}{\delta x_j \, \delta x_j} = \frac{1}{\Delta t} \frac{\delta \hat{u}_i}{\delta x_i} \equiv Q, \tag{8}$$

which is the discrete analogue of the Poisson equation. This equation is applied to all grid cells that are not adjacent to the boundaries. For the latter group of cells, the equations arising from the substitution of the internal velocity values in the discrete forms of the continuity equation are used (Kim & Moin 1985).

Expansion of ϕ and Q into one-dimensional discrete Fourier series and use of the trigonometric orthogonality property allows the transformation of (8) into

$$\left(\frac{\delta^2}{\delta y^2} + \frac{\delta^2}{\delta z^2}\right)\tilde{\phi} - \alpha^2 \tilde{\phi} = \tilde{Q}, \tag{9}$$

where the tilde denotes the one-dimensional Fourier coefficients and α is the modified wavenumber

$$\alpha^2 = 4 \frac{\sin^2(\frac{1}{2}\kappa_x \Delta x)}{\Delta x^2},$$

where κ_x and Δx are the streamwise wavenumber and grid spacing respectively.

For non-uniform grids, the solution of (9) requires the inversion of a block-tridiagonal symmetric matrix for each wavenumber. This is efficiently achieved with the use of the extended cyclic reduction algorithm due to Swarztrauber (1974). In the present implementation the solution for all wavenumbers is carried out simultaneously. This permits the vectorization of most steps in the solution procedure. There is, however, some loss of accuracy in the calculated results due to the slow growth of round-off errors. This tendency is inherent in the solution algorithm and thus unavoidable. This loss of accuracy (which was quantified above) on the computed velocities is thought to be unimportant when compared to the space and time truncation errors. The non-slip and periodicity boundary conditions on the velocity are enforced with the aid of a set of fictitious grid cells placed outside the computational domain.

The errors in the calculated velocity field of a laminar flow through a straight duct of square cross-section have been found to decrease at a rate proportional to the square of the grid size for both uniform and non-uniform grid distribution. However, the error found in the computed velocity at the four grid points closest to each of the corners tends to be large – about 10% and falling by more than an order of magnitude over the surrounding grid points – even though the error for a fixed position in the duct arbitrarily close to the corner always displays convergence. This is not thought to be a drawback because in the turbulent case the flow very close to the corner, and in particular near the first grid point, is quiescent. The results of the driven cavity test were identical to those obtained by Kim & Moin (1985).

The code was also adapted so that free slip (zero shear stress with no-through flow) could be applied to any one of the four solid boundaries. By setting one pair of opposite walls to non-slip conditions and the other to free slip, plane Poisseuille flow could be simulated. This arrangement was used to calculate the decay rates for two-dimensional Tollmien–Schlichting waves up to Reynolds number 2500 (based on the mean centreline velocity and channel half-width). For 128 streamwise and 127 uniformly distributed cross-stream grid intervals (which is the optimum for the present numerical scheme), the difference between the eigenvalues found from the simulated flow and those obtained from the numerical solution on the Orr–Sommerfeld equation was less than 3 %.

3. Numerical and flow parameters

From the practical point of view it is desirable to carry out the duct simulation at the highest possible Reynolds number. However, the choice of its value is severely constrained by physical and numerical considerations. For the simulation of turbulent bounded flows in general, it is necessary to represent the viscous sublayer where some of the structures associated with the generation of turbulent energy are thought to originate. The grid spacing normal to a boundary needs to be sufficiently fine to resolve the steep velocity gradients occurring there, whereas the spanwise grid should be sufficiently dense to capture the high- and low-speed streaks. For the duct flow, the coordinate direction normal to one pair of opposite walls corresponds to the spanwise coordinate of the other pair and vice versa. Thus, the grid spacing throughout the duct cross-section is determined by the resolution requirements near the boundaries. The cross-stream grid point distribution employed here was derived using the following transformation function:

$$x_i = h\left[1+\frac{\tanh(c\xi)}{\tanh(c)}\right], \quad -1 \leqslant \xi \leqslant 1,$$

where $2h$ is the length of the square duct side and the adjustable parameter c was used to fix the grid spacing nearest to each boundary. For the present computations $c = 1.8417$.

Another limiting factor arises from the streamwise lengthscales of the turbulent flow. It has been found necessary to make the streamwise extent of the computational domain very long to ensure that the two-point streamwise correlations of the velocity at all transverse positions have decayed sufficiently for separations equal to half the streamwise length. This is essential in order to approximate fully developed axial flow with the periodic boundary conditions along the mean flow direction; it was achieved at the expense of having a somewhat larger streamwise grid spacing.

Because the flow is driven by a constant pressure gradient, $\mathrm{d}P/\mathrm{d}x$, the average value of the friction velocity over the wetted area of the duct is given by

$$\bar{\tau}_w = u_\tau^2 = -\tfrac{1}{4}H\frac{\mathrm{d}P}{\mathrm{d}x}, \tag{10}$$

where H is the hydraulic diameter of the duct defined by

$$H = 4A/S,$$

with A the cross section area of the duct and S its perimeter length. For the square duct, $H = 2h$.

The Reynolds number based on the friction velocity and hydraulic diameter is $Re^+ = 300$. The computational domain has dimensions 20π (streamwise) $\times 2 \times 2$, or equivalently $9425 \times 300 \times 300$ in wall units (a wall length unit is defined as ν/u_τ and flow variables measured in these units will be denoted by the superscript +). The number of grid intervals along each direction is $1000 \times 127 \times 127$, which correspond to a streamwise grid spacing of $\Delta x^+ = 9.4$, and $0.45 < \Delta y^+, \Delta z^+ < 4.6$ for the cross-stream directions. As noted above, the rate of change of grid spacing is at most 6%. Because of the staggered grid arrangement the velocity components parallel to each wall are, at their closest, half the near-wall grid spacing, or 0.225 wall units. The computation with this set of parameters will be referred to below as the standard run. On a four-processor Cray-2 system the code takes, on average, 85 c.p.u. seconds for each time step and occupies 131 million words of core memory.

Owing to the explicit treatment of the advection terms, the time step Δt was restricted to a value satisfying

$$\mathrm{CFL}_{\max} = \Delta t \max\left[\frac{|u|}{\Delta x} + \frac{|v|}{\Delta y} + \frac{|w|}{\Delta z}\right] \leqslant 0.3,$$

which resulted in the choice $\Delta t = 0.054\,\nu/u_\tau^2$ (defined as wall time units) or equivalently $0.00036h/u_\tau$ (h/u_τ will be referred to as a turnover time). This gave an average value for the $\mathrm{CFL}_{\max}$ of 0.24.

The initial conditions for the simulated flow were derived from the velocity fields of two precursor simulations. In the first of these the dimensions of the computational domain were $8\pi \times 2 \times 2$. The starting field in this case was equal to the sum of a solution for laminar duct flow and a fluctuating velocity field derived from a random number generator. At first, the grid in the streamwise direction was chosen to be coarse whereas the cross-flow resolution was identical to that of the final calculation. The initially unphysical velocity field was allowed to relax for several turnover times and was subsequently transferred to a finer grid using Fourier interpolation. After successive x-grid refinements the grid spacing became identical to that of the final simulation. It was found that with the shortest domain the u-velocity fluctuations remained strongly correlated for the maximum possible separation. The simulation was then continued in a $16\pi \times 2 \times 2$ domain with identical grid resolution. The initial conditions for this run were set by copying the latest flow field from the $8\pi \times 2 \times 2$ simulation into one half of the new domain, and setting the remaining half to a laminar flow with the streamwise velocity field identical to the mean flow of the turbulent part. This ensured that the highly correlated precursor field was not carried into the successor simulation. After several turnover times the two-point velocity correlations at various cross-stream positions were calculated using space and quadrant averaging. These indicated that a 16π simulation would probably have been unaffected by the use of periodicity but it was felt safest to use a larger domain. The incremental cost of the computation would be partly offset by having a larger sampling volume and better vectorization. The velocity field was thus transferred, as before, into the final $20\pi \times 2 \times 2$ domain and was run until the fluctuating field had filled the whole domain. The simulation was continued for a further six turnover times, followed by five turnover times during which time-averaged statistics were

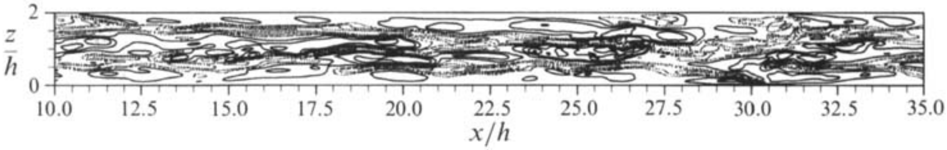

FIGURE 2. Contours of the instantaneous fluctuating component of u over an 8π section of a plane parallel to the $y = 2h$ wall (CD; see figure 1 for definition) and at a distance $y = 0.07h$ ($y^+ = 10.5$) from it. The mean flow is from left to right: —, positive values; · · · · ·, negative values.

accumulated. The maximum variation of the bulk velocity (U_b) over the latter part of the simulation was less 0.2 % of its mean value, while the corresponding figure for the volume-average kinetic energy was below 5 %.

Compared to the final simulation, the maximum intensities of streamwise velocity (u_{rms}) from the 16π and 8π simulations are 2 % and 6 % lower respectively. It would not be safe, however, to assign any definitive trend in these statistics. The uncertainties due to time-averaging are greater than the above differences, most notably in the 8π simulation where the integration time would need to be increased by a factor of at least 2.5 in order to compensate for the smaller computational box. Also, the velocity field generated when using the 8π domain is not a reliable source of physical information. Nevertheless, it may be of interest to note two more salient statistical features. One concerns the one-dimensional velocity spectra, notably that of u (not shown), which shows higher energy content in the low-wavenumber range of the 8π calculation compared with the same range of the 20π simulation. The total energy of each component is approximately the same. Thus, in both calculations similar amounts of energy are being extracted from the mean field but they differ in their distribution within their respective wavenumber ranges. It has also been found that the two-point u-correlations showed the slowest decay within $0.15h$ of the duct walls. Figure 2 shows contours of the instantaneous distribution of the fluctuating u-field at time $t = 11h/u_\tau$ from the 20π simulation. It is an 8π segment of a plane which is parallel to the $y = 2h$ wall (side CD on figure 1a) and at a distance $0.07h$ from it. It was chosen because it shows a meandering low-speed region (starting at $x = 10\,h$, $z = 1.5h$) spanning the whole length of the section as well as what may be called the merging of two low-speed regions near $x = 21h$. It may be conjectured that this could be one mechanism responsible for the generation of the longest low-speed streaks. Similar examples at earlier times were observed to break up.

The mean flow statistics were calculated by sampling in time the instantaneous streamwise-averaged flow variables. Fluctuating quantities were estimated with respect to the final mean values. To alleviate the core memory requirements during execution, the calculation of the two-point velocity correlations was restricted to the first quadrant only. All other statistics were calculated for the whole of the duct cross-section. Despite the great length of computational domain used, the averaging time was not sufficient to give completely (anti)symmetric variation in all statistics, though it was sufficient for unambiguously deducing all qualitative features of the flow field as well as quantitative statistics when quadrant averaging is used. To test if any of the asymmetry was due to coding error, a very low-resolution run was made – which was of no physical significance – for extremely long times. From this it was established that the code could produce statistics with appropriate symmetry or antisymmetry to within 1 %.

Because the strong sweep and ejection events are not necessarily perfectly aligned with the streamwise axis, their apparent duration along a line of grid cells parallel to the x-axis can be much shorter than the lifetime of the event itself. To avoid excessively long integration times the sampling period was small enough to capture such events. The sampling interval of $0.018h/u_\tau$, or every 50 time steps, was sufficiently small to capture the peaks in the time history of the Reynolds shear stresses near the duct walls. The mean secondary flow field is converged except near the wall bisectors.

The greater part of the viscous dissipation was found to occur in the mean field. Two thirds of the total dissipation was due to the mean u-field whereas less than 0.1% was due to the mean secondary flow. Assuming that the remaining third due to the turbulent field is uniformly distributed over the whole duct volume, the Kolmogorov dissipation scale will be close to 2 wall units. This is probably an underestimate of the magnitude of the smallest scales present in very low-*Re* turbulent flows with the same energy dissipation rate since in this case the viscous dissipation will be distributed over all scales rather than being concentrated in the smallest.

In order to test the sensitivity of the computed results to the grid size, two coarse-grid runs were made for shorter integration times. In both of these runs the streamwise length of the computational box was bigger (24π) but no flow parameters were changed. In the first – which will be referred to as run R1 – the grid was $768 \times 127 \times 127$, implying a 56% increase in Δx. The statistics from this run agreed well with the corresponding fine-grid data to within the averaging uncertainty, which was quantified from the asymmetry in the fine grid data. Some differences were observed in the streamwise spectra but only for wavenumbers corresponding to wavelengths less than $4\Delta x$ on the coarse grid. The energy contained in these high wavenumbers is very small with no apparent qualitative effect on other turbulent statistics. One example of the influence of coarser streamwise resolution on the flow is shown on figure 7 below. It shows the distribution of the wall stress, which is related to the secondary flow field, and indicates close agreement between the two simulations. The second run – run R2 – was made on a $768 \times 63 \times 63$ grid (the cyclic reduction algorithm used in solving (9) allows $2^m - 1$, m being an integer with $m > 2$, grid intervals). The cross-stream resolution of this run is too coarse for testing the grid convergence of the other calculations, but it was found useful in excluding the possibility that the cross-stream resolution might have had a decisive influence on the simulated secondary flow field.

The two-point velocity correlations for three different cross-stream positions are shown on figure 3. The (y, z) coordinate values refer to the position of the centre of the grid cell whose velocities are displayed. In figure 3 (a, c) the v- and w-velocities are symmetrically placed about the corner bisector. In the former the correlation curves are very similar whereas in the latter the similarity persists for relatively small separations with larger separations having small and apparently random variations. The lack of smoothness at larger separations in all figures is the result of insufficient time averaging. A comparison of the velocity correlations for cross-stream positions symmetrically placed about the corner bisector, but within the first duct quadrant – not shown – indicate that the waviness is not systematic. The curves shown are typical of those found in other cross-stream positions.

The results shown on figure 3 also suggest that the ratio of the length of the computational box to an integral lengthscale of turbulence in the duct is much greater than that found sufficient for the plane channel simulation of Kim, Moin & Moser (1987). Although the minimum duct length necessary is not at present known, the difference remains notable even if one considers that the length of the duct at the

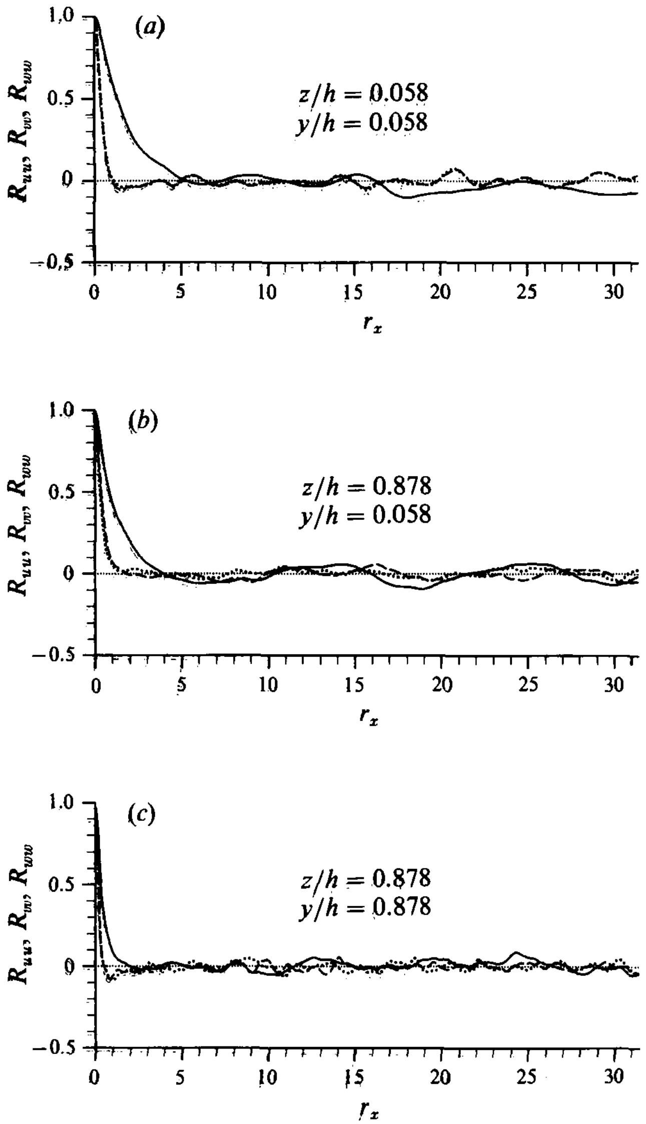

FIGURE 3. Two-point velocity correlation coefficients at three cross-stream locations: ——, u; · · · · ·, v; – – –, w.

present Reynolds number has to be greater than 8π. However, the results from the two simulations are not contradictory. The present results support the use of two-point correlations as sensitive means for detecting unphysical effects in short periodic domains, but also suggest that their use in predicting the minimum box length, without some prior knowledge about the flow field, is unsafe. This is compatible with the properties of the two-point correlations in relation to the underlying structure of turbulence as discussed by Townsend (1976). For example, his model of quasi-periodic structures in space (p. 10) can be made to account for the present findings in a period domain but it is not at present known if this model is appropriate.

4. The mean velocity field

The Reynolds number based on the bulk velocity U_b was $Re_b = 2hU_b/\nu = 4410$, with the volume-average turbulent kinetic energy having a time-mean value of $2.1u_\tau^2$. Variations in the instantaneous secondary flow field had no discernible influence on U_b. This may be one of the factors contributing to the success in predicting the friction factors in rectangular ducts of correlations adapted from circular pipe flows (Jones 1976). The friction factor for the square duct can be written as $f = 8u_\tau^2/U_b^2$. The simulation gives $f = 0.037$, the same as the value obtained from Jones' correlation

$$1/f^{\frac{1}{2}} = 2\log(Re_j f^{\frac{1}{2}}) - 0.8, \tag{11}$$

where Re_j is the modified Reynolds number which, for a square duct, is given by $Re_j = 1.125Re_b$. The agreement is excellent even though the present Reynolds number is near the lower limit of the experimental data that support Jones' correlation. Additionally, the ratio U_0/U_b, where U_0 is the mean centreline velocity, is near 1.33. This value is larger than those measured in higher Re_b duct flows but consistent with the trend found in the review part of the work by Demuren & Rodi (1984) which includes Lund's (1977) value of 1.25 for $Re_b = 25000$ – the lowest – Re_b data included in their figure 2. Evidence for the presence of a core flow region in the simulation can be seen in figure 4(*a*), which shows the variation of mean streamwise velocity, U^+, along the diagonal (AC). The steeply varying velocities possess inflexion points each at a distance $0.13h$ along the diagonal from their respective corners. This feature is also found in the profiles of fully developed laminar duct flows. Four additional inflexion points are also present in the flatter top part of the velocity distribution in figure 4(*a*) and are symmetrically placed about the centreline, but they are difficult to discern. Figure 4(*b*) shows the variation of U/U_0 along the normal bisector and includes the low-*Re* plane channel measurements of Nishino & Kasagi (1989) and Niederschulte (1989) (for his Reynolds number 2457 based on the bulk velocity and the channel half-width), for comparison. Relatively smaller flow velocities are found in the duct near $y/h = 0.25$, this being the effect of the secondary flow.

A short experimental study of the turbulent flow through a square duct has recently been carried out by Cheesewright, McGrath & Petty (1990). Their Reynolds number based on the centreline velocity and duct side was $Re_0 = 2hU_0/\nu = 4900$ which is close to that of the simulation, 5880. In this experiment a fibre optic LDA technique was used to measure the streamwise and horizontal velocity statistics in air seeded with smoke particles. The measurements for the streamwise velocity were carried out 0.078 hydraulic diameters downstream of the duct discharge exit plane whereas the horizontal velocity statistics were obtained 0.64 hydraulic diameters upstream of the exit plane. The latter was situated about 100 hydraulic diameters downstream of the inlet trip device. There is therefore some uncertainty associated with the measured velocities and in particular with the moments of the streamwise component near the assumed duct boundaries. Figure 5(*a*) shows a comparison between the measured values of U/U_0 (U_0 is the only velocity scale available from this experiment) and those derived from the simulation by averaging the time statistics over the four quadrants. The agreement between measurements and simulation for points in the flow at distances greater than $0.2h$ from the nearest wall is excellent. Outside these limits the measured U-values are quite asymmetric with respect to the corner bisector with velocities differing by as much as 20%. Comparison between the measured and quadrant-averaged values of W is made in figure 5(*b*). Because the simulation results are symmetric to within 4% it is inferred

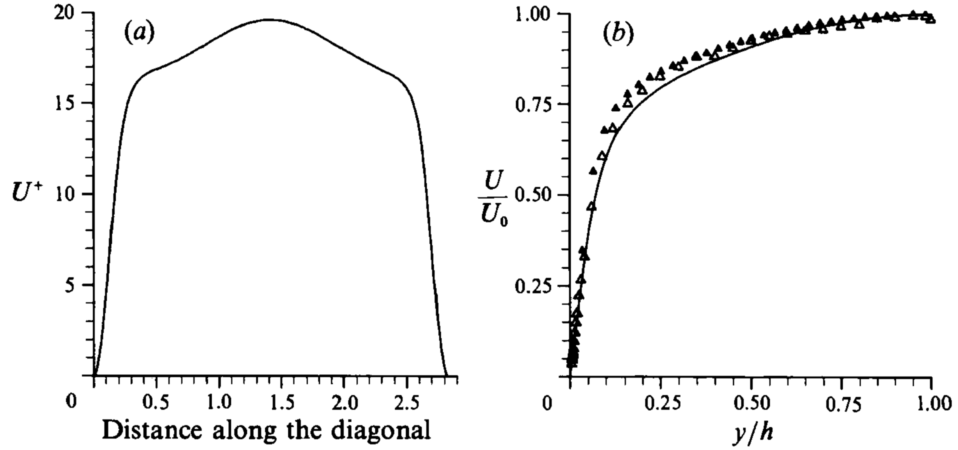

FIGURE 4. Mean streamwise velocity distribution (*a*) along the diagonal AC, and (*b*) comparison with plane channel data: ——, U-velocity from the duct simulation along the wall bisector. Plane channel data: △, Niederschulte (1989); ▲, Nishino & Kasagi (1989).

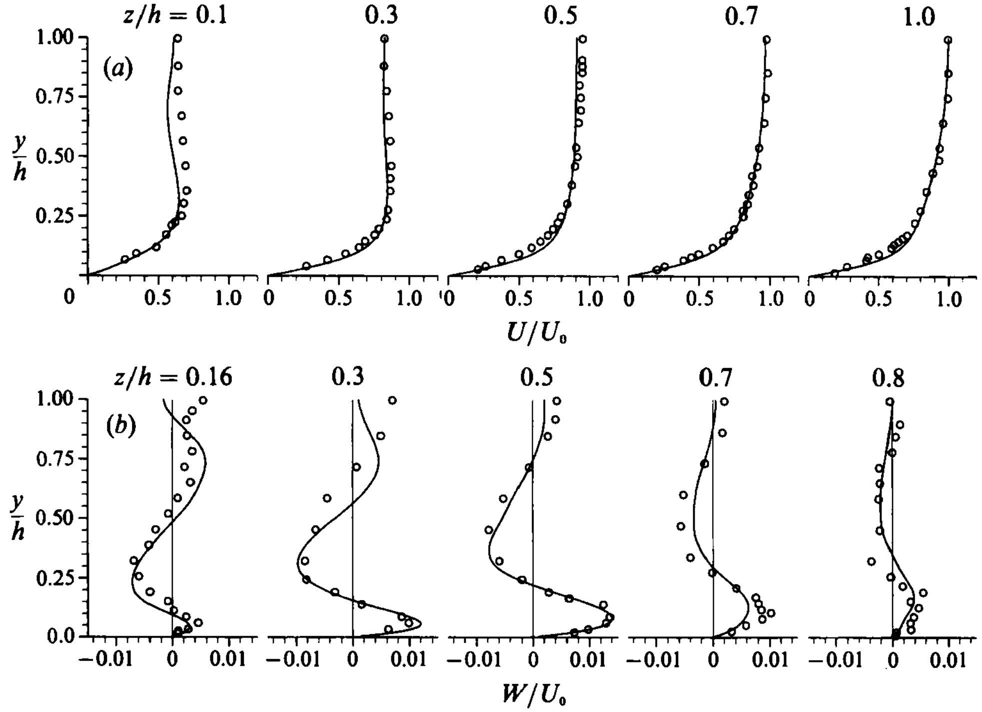

FIGURE 5. Comparison of the simulated mean (*a*) streamwise and (*b*) spanwise velocity profiles with the square-duct measurements of Cheesewright *et al.* (1990): ——, quadrant-averaged simulation data; ○, experiment.

– by comparing the zero crossings of the two sets of data – that the secondary flow cells of the experiment are also asymmetric about the corner bisector.

The mean secondary flow field is shown in figure 6. In figure 6(*a*) the U-isovels have been superimposed on the vector field, showing the correspondence between the two sets of flow statistics. Although some asymmetry in these results is still evident, the

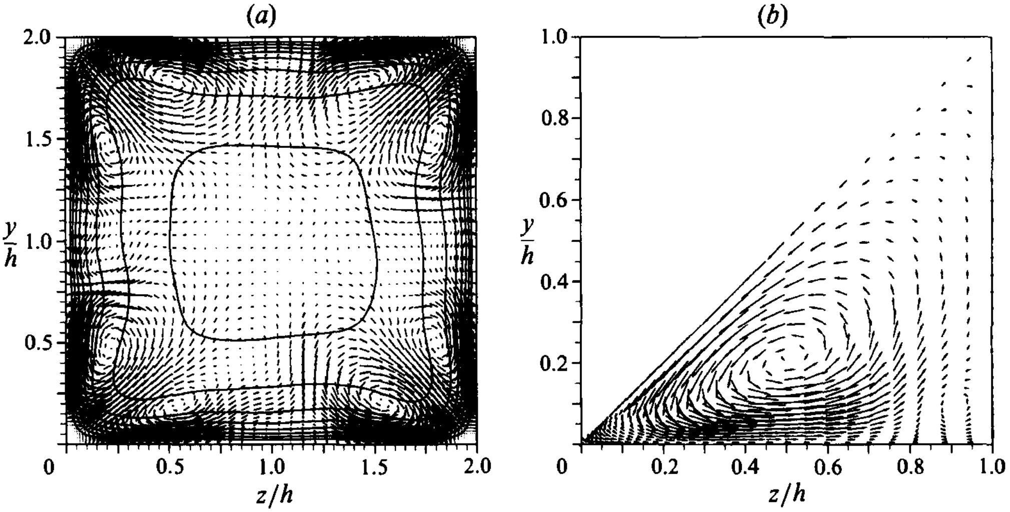

FIGURE 6. (*a*) Mean secondary velocity vectors and mean streamwise flow contours. The contour increment is $4u_\tau$ with the lowest value contour being nearest to the duct walls representing $4u_\tau$ units. (*b*) Vector field in (*a*) averaged over all octants. Only half the vectors in each direction are shown.

main features of the flow are uniformly present. Moreover, comparisons with data from run R1 show that the asymmetry found in figure 6(*a*) is not systematic. The distribution of U across the duct cross-section is seen to conform with the expected effects of the secondary flow field. The distortion of the isovels towards each corner is due to the momentum transfer by the secondary velocities towards that corner. The mean cross-stream flow does not however extend to or remain close to the walls as far as the wall bisectors, and the isovels are found to bulge toward the wall around the wall bisectors where the secondary flow field lacks symmetry. To overcome this, the secondary flow on figure 6(*a*) has been averaged over all octants and is shown in figure 6(*b*). The maximum secondary velocity thus calculated is 1.9% of the bulk velocity and it is found at $y/h = 0.071$, $z/h = 0.45$ or $y^+ = 10.65$, $z^+ = 67.5$. Even though there is some uncertainty as to the appropriate velocity scale near the corner, it is evident that the maximum secondary velocity occurs just outside the wall viscous sublayer rather than on the corner bisector. An unexpected feature of figure 6(*b*) is the presence of a smaller flow cell near the wall bisector with a maximum velocity in this cell well below 1% of the bulk velocity and with its centre below $y/h = 0.1$ ($y^+ = 15$). These flow features give rise to the average wall stress (τ_w) distribution shown in figure 7. This shows two wall stress peaks due to the larger secondary flow cells at a distance $0.31h$ from the nearest corner and a third one in the middle of the duct wall. The contribution of the spanwise stress component is very small. The angle of the wall stress vector with the x-axis is at most 3°. The average wall stress over the four walls and its value calculated from the mean pressure drop differ by less than 0.1%. This distribution of the wall stress has not been observed in higher-Reynolds-number experiments in square ducts although it has been found in turbulent flows through rectangular ducts at some higher aspect ratios (Leutheusser 1963; Knight & Patel 1985; Nezu, Nakagawa & Tominaga 1985).

It is of some importance to ascertain the sensitivity of the wall stress distribution to the numerical parameters of the simulation. Firstly, there is the possibility that the duration of the time-averaging phase of the simulation is not sufficient. This

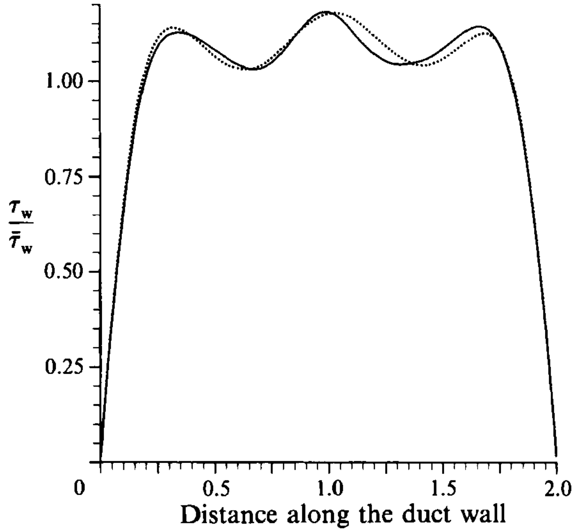

FIGURE 7. Wall stress variation. Four-wall-averaged distribution: —, standard run; ·····, lower-resolution run (run R1 in §3).

appears unlikely since the wall stress distribution has been found to be the same for all four walls, with similar results from the precursor simulations. Some very short time averages and instantaneous streamwise averages have been found to have a wall stress minimum at some of the wall centres but apparently these do not survive in the mean. Another important consideration is the effects of the grid size and distribution. A substantial increase in the streamwise grid spacing Δx, run R1, gives results very similar to those of the standard run: figure 7. With run R2 both the grid spacing and the rate of grid change in the cross-stream directions are quite different from those of the standard run but the computed mid-wall stress has been found to be an attenuated local maximum suggesting that further coarsening of the cross-stream grid will suppress the mid-wall maximum of the stress. There is therefore no apparent sensitivity of the wall stress distribution derived from the simulation on the grid used. It also worth mentioning at this point a possibly fundamental difference between simulated and measured duct flows. In the former, the computed secondary flow is not contaminated with upstream influences. It is however possible that the measured secondary flows are a mixture of the turbulence-generated flow and structures convected from the developing part of the duct. This is one possible explanation for the asymmetries in the mean velocity data of Cheesewright *et al.* (1990).

The average value of the four mid-wall stresses obtained from the simulation is approximately $1.18\bar{\tau}_w$ (the same value was obtained from run R1). The work of Popovich & Hummel (1967) suggests that the local maximum may be detectable. These authors used a non-intrusive visualization technique to obtain 147 samples for the instantaneous velocity gradient at the mid-point of the wall of a square-duct turbulent flow. Their Reynolds number based on the bulk velocity and the hydraulic diameter was 13100, which is about three times the present value. The mean wall stress for the experiment was calculated indirectly from the mean flow rate on the assumption that the friction factor for the duct was the same as that of a round pipe at the same Reynolds number. This estimation gave a value for their $\bar{\tau}_w$ below the local stress value inferred from the mid-wall flow visualization, but it is also possible

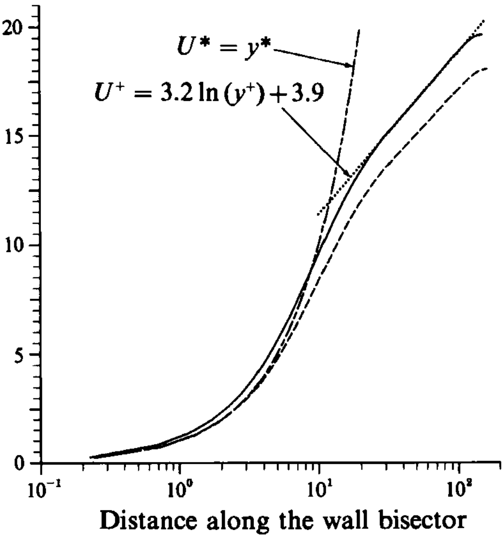

FIGURE 8. Logarithmic plot of the quadrant-averaged streamwise velocity using two different velocity scales: ——, scaling based on u_τ; ---, scaling based on the mid-wall value u_*.

to derive a more appropriate estimate for $\bar{\tau}_w$ from Jones' correlation for square-duct flows (equation (11)). With respect to the latter estimate for the mean wall stress, the measurements of Popovich & Hummel imply that their mid-wall stress is equal to $1.15\bar{\tau}_w$, which is in good agreement with the result of the simulation. The factor 1.15 corresponds to the authors' preferred estimate for the mid-wall stress, but the reported measurements show that alternative estimates within 7 % of this value are possible.

Of the three velocity scales available, namely U_0, U_b and u_τ, the friction velocity is usually deemed the most suitable choice for bounded turbulent flows since its value can be directly related to the turbulent stress field. The variation of the local mean wall stress, and therefore the local friction velocity, over the duct boundaries introduces an ambiguity as to which scale should be used. Within the viscous sublayer the local value is the correct choice. For the flow field near the streamwise axis of the duct the mean value defined by (10) is more appropriate. Furthermore, it is not obvious how the transition between the mean and local values should take place. In figure 8 the variation of quadrant-averaged U is shown with two different velocity scales: u_τ and the mid-wall value u_* (in the following the superscript * will be used to denote quantities scaled using local values of the friction velocity). The latter scaling is expected to be valid for some distance beyond the viscous sublayer as the distortion of the isovels on figure 6(*a*) suggests. Both scalings show logarithmic regions. The logarithmic region on the u_τ-scale follows the relation $U^+ = 3.2\ln(y^+)+3.9$ over the range $30 < yu_\tau/\nu < 100$. The constants in this approximation of the logarithmic law are quite different from the accepted values of 2.5 and 5.0 respectively for high-Reynolds-number flows near boundaries. In low-Reynolds-number flows, a better value for the latter constant is 5.5. The corresponding duct value is well below that, indicating a stronger influence of the secondary flow field on U.

5. Statistics of the turbulent field

In the experimental work of Wei & Willmarth (1989) and of Teitel & Antonia (1990) on plane channels at low Reynolds number, it was observed that the effects of a bursting event near one of the boundaries can sometimes be detected in the vicinity of the other. This finding suggests that there may be important differences underlying the turbulent boundary layer and plane channel (which below will be referred to simply as channel) flow measurements. In order to minimize the sources of uncertainty in the following comparisons, additional data from published channel flows only will be used.

The variation of the flow statistics along one of the wall bisectors of the duct will first be compared with their cross-stream variation in channels. The mean flow along each wall bisector has no component normal to it, a condition similar to zero mean spanwise flow in a channel, although there is a non-zero component parallel to the wall bisectors over most of their length. The influence of the walls parallel to each bisector is also quite strong. Another difference with channel flows is that symmetry requires that the cross-stream velocity statistics at the centre be the same. In this respect, conditions at the centre of the duct are closer to those near the centre of a circular pipe.

Owing to the staggering of the velocities in space, the spanwise velocity component has no value defined on the normal bisector but at its nearest it has values at a distance of 2.3 wall units from the bisector. With the quadrant averaging which will be used below, only one set of values close to the normal wall bisector is available.

The equation for the mean streamwise momentum can be written as

$$-\frac{\partial UV}{\partial y}-\frac{\partial\langle u'v'\rangle}{\partial y}-\frac{\partial UW}{\partial z}-\frac{\partial\langle u'w'\rangle}{\partial z}+\nu\frac{\partial^2 U}{\partial y^2}+\nu\frac{\partial^2 U}{\partial z^2}=\frac{\mathrm{d}P}{\mathrm{d}x}, \tag{12}$$

where $u = U+u'$ with u' being the fluctuating velocity and with similar definitions for the other two velocity components. The operator $\langle\ \rangle$ is used to denote the average of the enclosed quantity, which in the simulation is obtained by space and time averaging (§3). The terms of this equation represent the mean forces per unit mass acting at a point in the fluid. The sum of all terms at various cross-stream positions has been found to equal – to within 5% – the pressure term on the right-hand side of (12).

The distribution of the quadrant-averaged Reynolds stress $\langle -u'v'\rangle$ scaled with the similarly averaged mid-wall stress is compared with the simulation results of Kim *et al.* (1987) and the measurements of Nishino & Kasagi (1981) and Niederschulte on figure 9(*a*). The smaller gradients between the duct wall and the maximum of $\langle -u'v'\rangle$ at $y/h = 0.2$ can be accounted for by the contribution of the other terms in (12), but beyond it the scaling based on u_* becomes progressively inappropriate. Because the viscous terms are negligible near the centre of the duct, symmetry requires that at the centre

$$h\frac{\partial\langle u'v'\rangle}{\partial y}=h\frac{\partial\langle u'w'\rangle}{\partial z}=u_\tau^2,$$

where use was made of definition (10).

The variation of the correlation coefficient between u and v is shown on figure 9(*b*). For $0.3 < y/h$ the experimental values for the coefficient tend to be below those of the Kim *et al.* (1987) and duct simulations. A near-wall maximum is evident in both

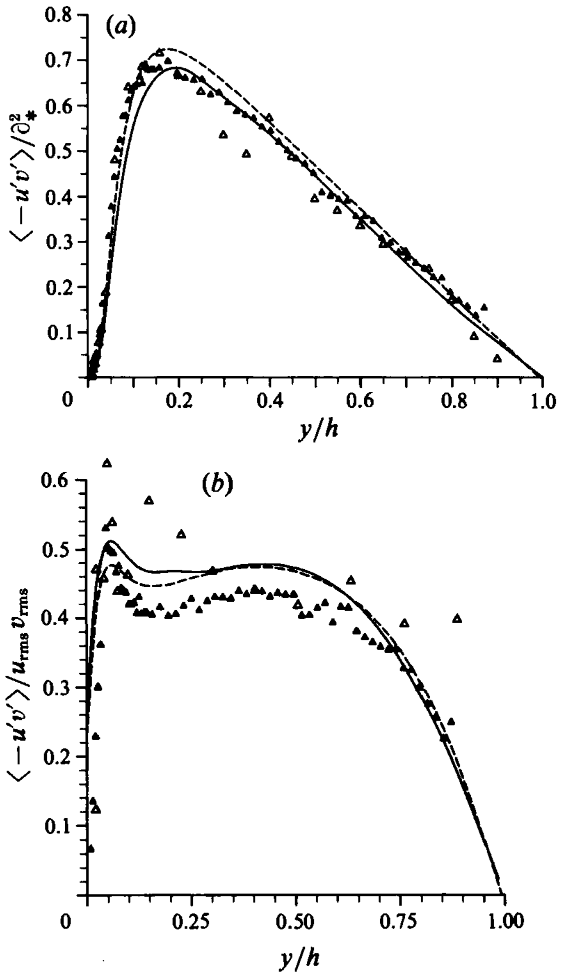

FIGURE 9. (*a*) Distribution of the primary Reynolds stress $\langle -u'v' \rangle$, and (*b*) correlation coefficient of u and v. —, Quadrant-averaged simulation data along the duct wall bisector; ---, Kim *et al.* (1987) plane channel simulation; △, Niederschulte (1989); ▲, Nishino & Kasagi (1989).

simulations, with the peaks occurring near $y^* = 9$ and 10 for the duct and channel respectively. The channel measurements also suggest the presence of a near-wall peak but the scatter within and between experiments prevents any quantitative inference. For $y/h < 0.25$ ($y^* < 40.5$) the correlation coefficient for the duct flow indicates a stronger organization of the turbulent field than in the simulated channel flow.

The velocity-scale dilemma is again encountered when comparison of the duct intensities (r.m.s.) is made with channel data. Figure 10(*a*) shows the variation of u_{rms} scaled with its local u_* value where in this case $u_*/u_\tau = 1.09$. The peak value of the u-intensity in the duct is found to be about 4% below the simulated and experimental values, except for the Kreplin & Eckelmann (1979) measurements which have a larger peak value than any of the other datasets. Near the streamwise symmetry axis both simulations predict lower intensities but it is noted that if u_τ were used with the duct data, close agreement would be found outside the viscous sublayer ($y^* > 5$). Similar comments apply to figure 10(*c*) on the w-intensity. The

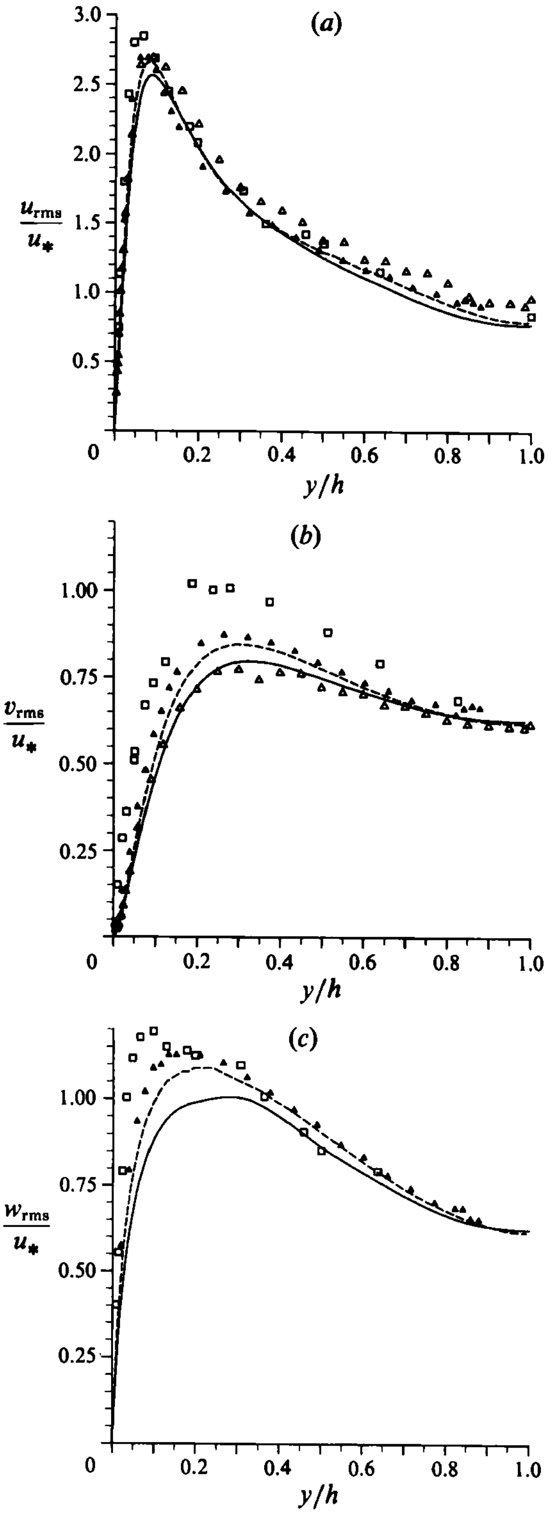

FIGURE 10. Comparison of the turbulence intensities between plane channel and square-duct simulation: (*a*) $u_{\rm rms}$; (*b*) $v_{\rm rms}$; (*c*) $w_{\rm rms}$. ——, Quadrant-averaged simulation data along the duct wall bisector; ---, Kim *et al.* (1987) plane channel simulation; △, Niederschulte (1989); ▲, Nishino & Kasagi (1989); □, Kreplin & Eckelmann (1979).

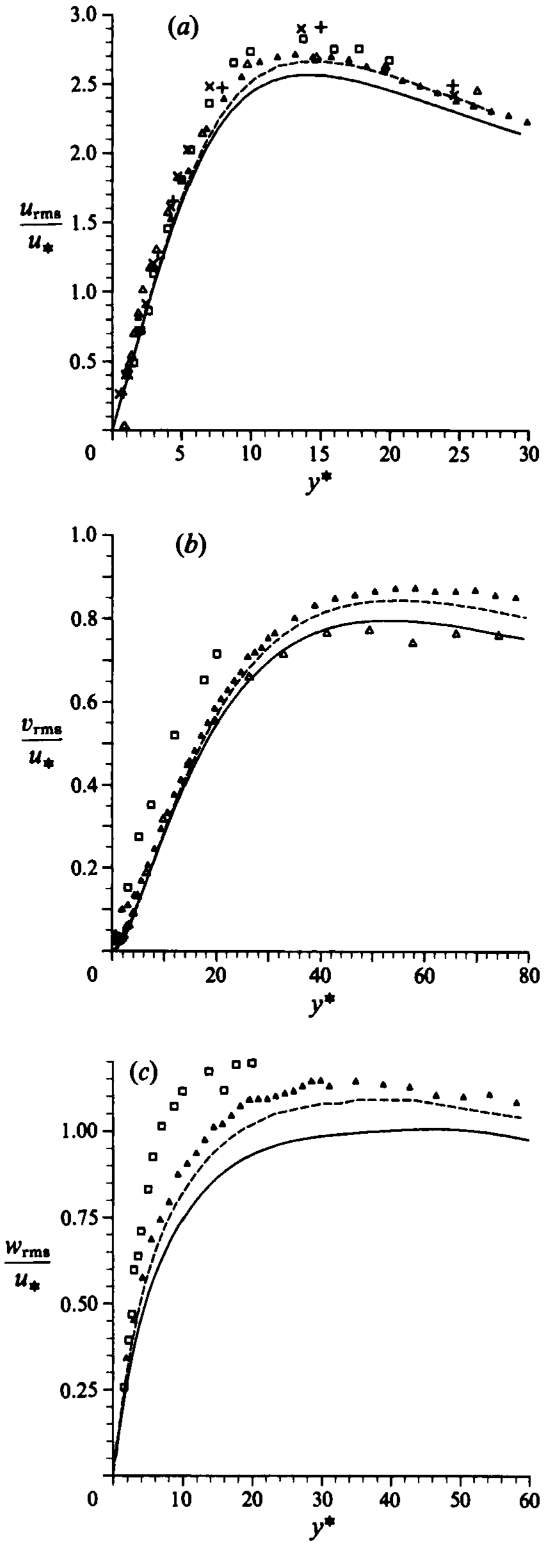

FIGURE 11. Turbulent intensities near the wall: (*a*) u_{rms}; (*b*) v_{rms}; (*c*) w_{rms}. Legends as in figure 10. Additional plane channel data from Alfredsson *et al.* (1988): +, $Re_0 = 5000$; ×, $Re_0 = 3800$.

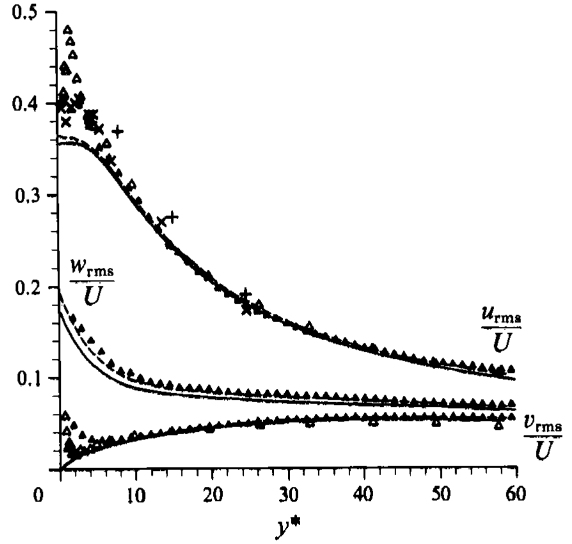

FIGURE 12. Variation of the turbulent intensities scaled with the local mean streamwise velocity. For legend see figures 10 and 11.

variation of intensity of the normal component v in figure 10(b) falls within the scatter of the experimental data. The near-wall variation of the intensities is shown on figure 11. Additional experimental data have been included in the figure for u_{rms} taken from the paper by Alfredsson *et al.* (1988). The data for the $Re_0 = 3800$ (based on the centreline velocity and the separation of the channel walls) experiment were obtained by them from the same oil channel facility as in Kreplin & Eckelmann (1979), whose data tend to support the earlier findings. For this reason rescaling of the Kreplin & Eckelmann data with a higher friction velocity, as in Kim *et al.*, was not adopted here. For $y^* < 5$ the simulations agree closely with Kreplin & Eckelmann (1979) but the other datasets show steeper u_{rms} gradients in the viscous sublayer. Consensus between the computations and available data on w_{rms} is confined to within the viscous sublayer. Good agreement is found in the near-wall v_{rms} variation, $y^* < 20$, with the exception of the Kreplin & Eckelmann's (1979) data.

The limiting values for u_{rms}/U and w_{rms}/U on the boundary are equal to the wall values of the root-mean-square of the spanwise, ω_z, and streamwise, ω_x, vorticity scaled with wall variables. For the duct data in figure 12 the implied velocity scale is the mid-wall friction velocity u_*. The measurements by Alfredsson *et al.* (1988) and Nishino & Kasagi (1989) suggest a value of 0.4 for the spanwise component, with the curves from the computations tending to boundary values around 0.36. Alfredsson *et al.* also used Popovich & Hummel's (1967) duct data to find that the non-dimensional r.m.s. of ω_z at the wall is 0.38. The w_{rms}/U ratio from the simulations is found to approach the wall with a noticeable slope although this would not be expected with higher grid resolutions since both w_{rms} and U have a linear dependence on y very close to the wall. The value of w_{rms}/U at the grid point nearest to the duct wall $y^* = 0.24$ is 0.17. The quadrant-averaged r.m.s. variation of the three components of the fluctuating vorticity along the wall bisector is shown in figure 13.

The near-wall asymptotic behaviour of the three components of the intensity and shear Reynolds stress is shown in figure 14. The streamwise intensity of both

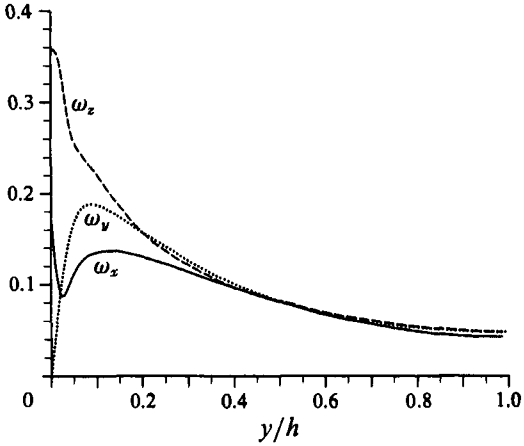

FIGURE 13. Root-mean-square vorticity fluctuation along the duct wall bisector. The results are the average intensities over the four duct quadrants: ——, $\omega_x \nu/u_*^2$; ·····, $\omega_y \nu/u_*^2$; ---, $\omega_z \nu/u_*^2$.

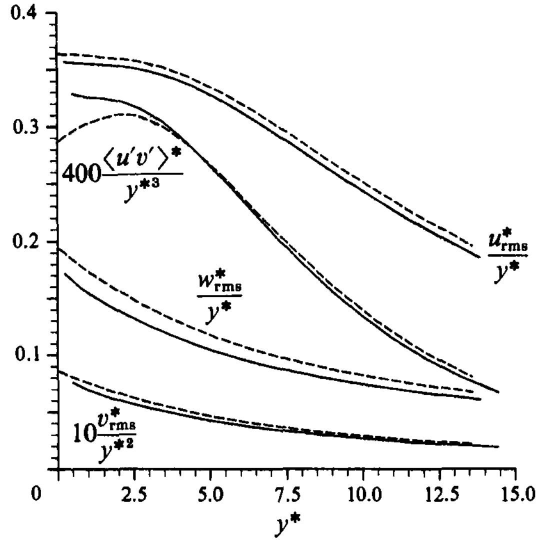

FIGURE 14. Wall limiting behaviour of the normal and primary shear stresses: ——, quadrant-averaged simulation data along the duct wall bisector; ---, Kim *et al.* (1987) plane channel simulation.

simulations shows linear variation below $y^* = 2$. The other two intensity components are found to follow their expected wall-limit variation only approximately. The results from the modelled boundary-layer work of Chapman & Kuhn (1986) suggest that the normal intensity exhibits quadratic variation with the distance from the wall for y^* less than 0.3 although their figures show that this can be considered to be approximately true as far as $y^* = 1$. Fitting the expected limiting relation of the cross-stream intensity to the appropriate value at the grid point nearest to the duct wall, it is found that $v^*_{\mathrm{rms}} = 0.0076y^{*2}$.

Asymmetry due to insufficient averaging was most pronounced in the higher-order velocity statistics. For this reason in the rest of this section quadrant-averaged data only will be used. The four-wall-averaged skewness and flatness velocity values at the

	Distance from nearest wall y/h	Skewness	Flatness
u	0.0015	0.95	4.17
v	0.003	−0.07	15.4
w	0.0015	—	6.5

TABLE 1. Values of the higher-order velocity statistics at the mid-wall grid point of the duct

grid nearest to the mid-wall are given in table 1. The w refers to the spanwise velocity whereas v is the normal component whose value has been defined as positive when the fluid moves away from the boundary. It is also noted that because of staggering $S(w)$ is defined slightly off the duct bisector where $S(w) = 0$ due to symmetry applies.

Except for $S(v)$, the values shown in table 1 are within 5% of those obtained from run R1. Because of the linear dependence of the instantaneous u- and w-components on y well inside the viscous sublayer, the skewness and flatness factors of u at the first grid point are equal to the skewness and flatness of the fluctuating streamwise stress at the wall. For these quantities Alfredsson *et al.* reported the values of 1.0 and 4.8 as best representing their measurements. The former value is in excellent agreement with the present computations, and good agreement is found between the flatness factors.

The influence of the sidewalls on the calculated velocity statistics along the normal is quite different for each velocity component. The fluctuations in u at the duct centre could have their origin in events near any of the four walls and on average each wall is of equal significance, whereas in the proximity of any wall the direct influence of the others would be small. Ejection events from the sidewalls are also expected to have a weak v-component and therefore to make no significant contribution to the statistics of v along the normal bisector. Conversely, the sidewalls will have a greater influence on the w-statistics near the duct centre.

The skewness data from three channel experiments and simulations are compared in figure 15. The measured values were obtained using three different measuring techniques and show considerable scatter. The $S(v)$ variation in the duct is closest to the hot-wire measurements of Kreplin & Eckelmann (1979) for $z/h > 0.3$ with skewness values nearer to the Gaussian distribution than the other channel data. However, the more recent measurements of Nishino & Kasagi (1989) and Niederschulte indicate that $S(v)$ is greater than the hot-wire measurements seem to suggest. It is noted that numerical diffusion may also be a contributing factor in reducing the skewing of v in the duct results, but the lower-resolution runs (§3) indicate that the differences in $S(v)$ compared with the channel data are, for the greater part, genuine. Near the wall $S(v)$ crosses the zero axis near $y^* = 40$, reaching a minimum of about -0.4 at $y^* = 11$ and remaining negative within the viscous sublayer.

A direct comparison of the intensities from simulation and square-duct experiments is made in figure 16. The measurements of Yong (1988) along the wall bisector of a square duct at $Re_b = 10000$, are also included. They were extracted from the appropriate figures of his thesis. For the wall bisector, $z/h = 1$, Cheesewright *et al.*'s (1990) experiment shows a maximum value for u_{rms}/U_0 noticeably larger than that from the simulation. Because the difference in the Reynolds number between that experiment and present simulation is small, the maximum u_{rms}/u_* for the former is expected to be well above any of the plane channel data shown in figure

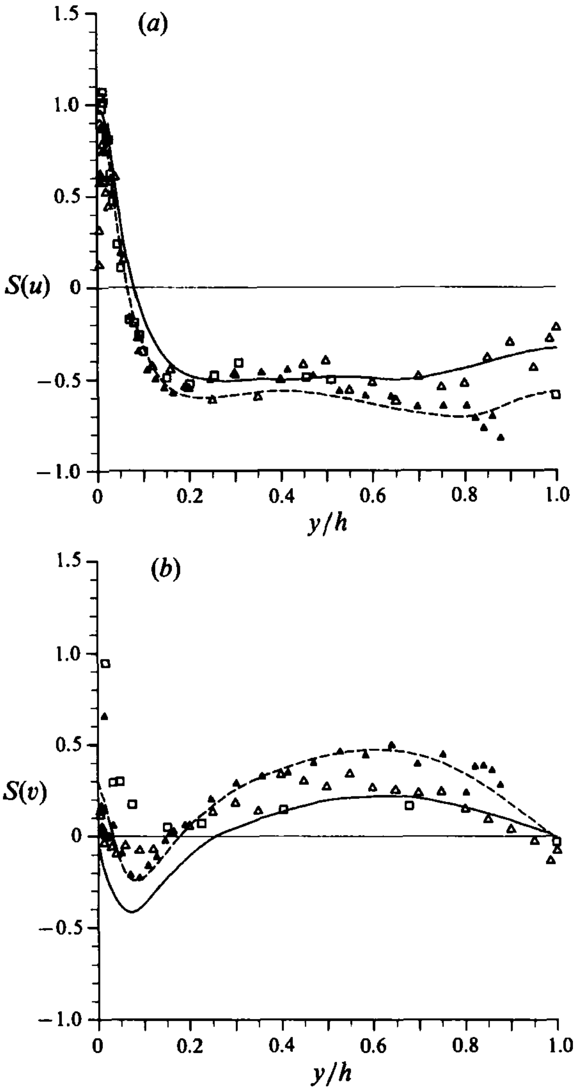

FIGURE 15. Velocity skewness factors along the wall bisector in global coordinates: (*a*) *u*; (*b*) *v*. Legend as for figure 10.

10(*a*). A possible explanation for this difference – suggested by H. Alfredsson (private communication) – is that owing to the flow expansion at the duct exit the measured values of U would be below those for the confined flow even though the turbulent structures would not alter significantly. This would lead to overestimates for the measured intensity of u. Overall, the data of Cheesewright *et al.* show noticeably higher u_{rms}/U_0 values at distances greater than $0.4h$ from the duct centre. The peak u_{rms} value found in Yong's measurements is in apparent agreement with the Cheesewright *et al.*'s measurements. If the u_τ scale had been used, however, then Yong's and the simulation maxima would both be $2.8u_\tau$ and located at $y^+ = 12$ and 13 respectively. Moreover, it would have been preferable to use the local velocity scales, but these were not available from the experiments. Excellent agreement between Cheesewright *et al.*'s and the simulation data for w_{rms}/U_0 is found over the duct quadrant, figure 16(*b*).

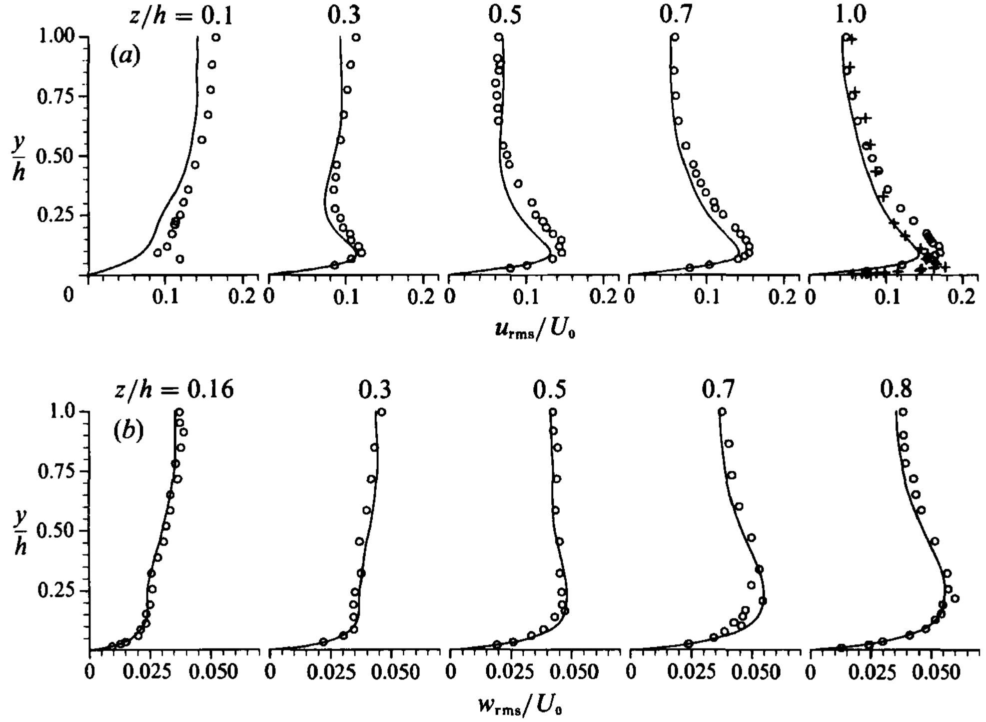

FIGURE 16. Velocity intensities across a duct quadrant: (*a*) u_{rms}/U_0; (*b*) w_{rms}/U_0. ——, Quadrant average from duct simulation; ○, Cheesewright *et al.* (1990); +, Yong (1988).

6. The mean streamwise vorticity

Most theories about the origins of the mean secondary flow have been built around the Reynolds-averaged Navier–Stokes equations and/or equations derived from them. A particularly concise example of this approach is the equation for the mean streamwise vorticity which for a fully developed duct flow reads

$$V\frac{\partial \Omega}{\partial y}+W\frac{\partial \Omega}{\partial z}+\frac{\partial^2}{\partial y\,\partial z}(\langle w'^2\rangle-\langle v'^2\rangle)+\left(\frac{\partial^2}{\partial y^2}-\frac{\partial^2}{\partial z^2}\right)\langle v'w'\rangle-\nu\left(\frac{\partial^2}{\partial y^2}+\frac{\partial^2}{\partial z^2}\right)\Omega=0, \quad (13)$$

where

$$\Omega=\frac{\partial W}{\partial y}-\frac{\partial V}{\partial z}$$

is the mean streamwise vorticity. The first two terms on the left-hand side have the familiar convective form found in the original Navier–Stokes equations, representing the convection of the mean vorticity by the secondary flow itself. The analogy between the viscous terms is more restricted (Morton 1984), but the effect of the last term of (13) is the tendency for viscosity-mediated reduction in gradients of Ω. The two terms involving the Reynolds stresses may, generally, be described as sources of vorticity. The first is associated with the vorticity production due to gradients in the anisotropy of the cross-stream normal stresses. The significance of the second has not always been recognized in modelling work; it may act as a production or dissipation term for Ω. The modelling of such flows involves finding appropriate prescriptions for calculating the Reynolds stresses rather than making direct use of (13), although any model must be consistent with the vorticity equation since it is an exact result of the equations of motion.

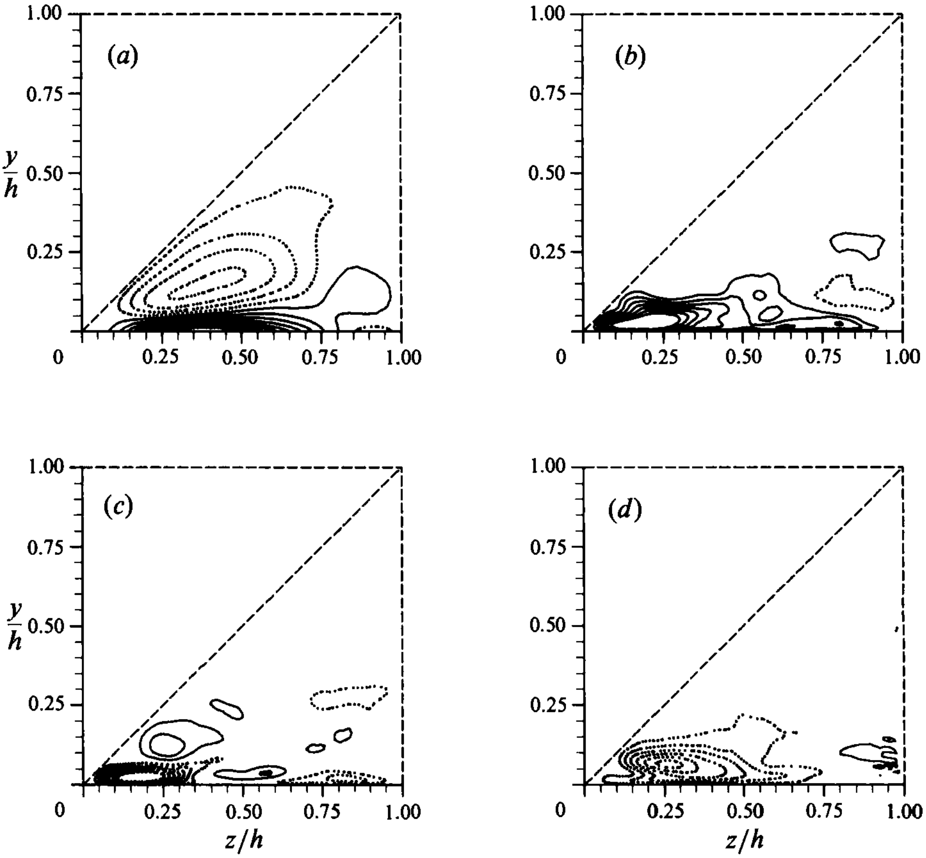

FIGURE 17. The distribution of the mean streamwise vorticity and the three dominant terms of the governing equation. All results are averaged over all octants and scaled with h and u_τ: (*a*) mean streamwise vorticity Ω, increment 1 and minimum contour -3.5; (*b*) anisotropy term: $\partial^2/\partial y\, \partial z(\langle w'^2\rangle - \langle v'^2\rangle)$, increment 3; (*c*) secondary stress term: $(\partial^2/\partial y^2 - \partial^2/\partial z^2)\langle v'w'\rangle$, increment 3; (*d*) Viscous diffusion: $\nu(-\partial^2/\partial y^2 - \partial^2/\partial z^2)\Omega$, increment 3. Continuous lines are used for positive values and dotted lines for negative.

The finite-difference form of the terms in (13) has been calculated from the simulated flow field and the distributions of the three terms most dominant near the corner, with additional averaging over all octants, are shown in figure 17. The mean streamwise vorticity Ω, computed from the vector field of figure 6(*b*), is shown in figure 17(*a*). The positive x-axis is directed into the plane of these figures and therefore the vorticity at the centre of the larger flow cell is a negative minimum. From this point the vorticity increases as the wall is approached, and attains a positive maximum on the wall itself. The change in sign occurs about 7 viscous lengths away from the lower wall. The value of the maximum Ω at the wall is more than twice the magnitude of the minimum at the centre of the primary cell. The spatial distribution of the stress anisotropy is shown in figure 17(*b*); its greatest contribution is in the production of positive mean vorticity near the corner at $y/h = 0.02$, $z/h = 0.19$ or $y^+ = 3$, $z^+ = 28$. Very close to it, $y/h = 0.025$, $z/h = 0.19$ in figure 17(*c*), the minimum of the secondary stress term is situated, with an absolute value about 10% less than the production maximum. The diffusion term has also a minimum, but it is further away from the corner: $y/h = 0.19$, $z/h = 0.25$ in figure 17(*d*).

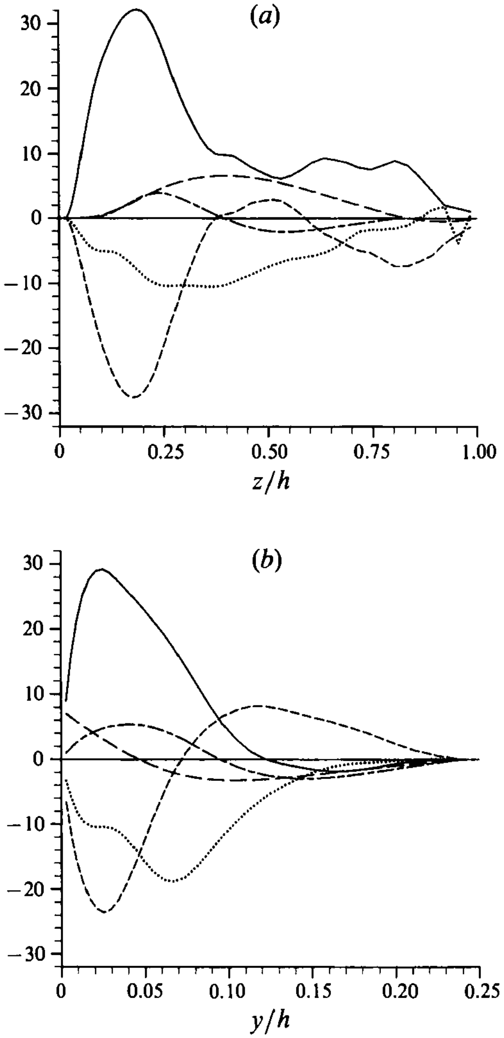

FIGURE 18. The variation of mean streamwise vorticity and the terms of its equation of motion along: (a) a line parallel to the z-axis at distance $y/h = 0.017$, (b) a line parallel to the y-axis at a distance of $z/h = 0.24$ terminating on the corner bisector. ——, Ω; ——, $\partial^2/\partial y\partial z(\langle w'^2\rangle - \langle v'^2\rangle)$; – – –, $(\partial^2/\partial y^2 - \partial^2/\partial z^2)\langle v'w'\rangle$; ·····, $\nu(-\partial^2/\partial y^2 - \partial^2/\partial z^2)\Omega$; — — —, $V\partial\Omega/\partial y + W\partial\Omega/\partial z$.

A more direct comparison between all terms is made in figure 18. In figure 18(a) the variation of Ω and the terms of (13) along a line parallel to the z-axis and at a distance $y/h = 0.017$ ($y^+ = 2.55$) is shown. The vorticity remains positive for the most part, except near the wall bisector. The anisotropy term is the main contributor to the production of positive vorticity throughout the spanwise length of the viscous sublayer; the viscous and shear stress terms act mostly as sinks of positive vorticity (two grid values of the former term near the bisector are in error: two columns of the diffusion term have been lost during the computation). The convection term makes only a small positive contribution just beyond the maximum of the production, with a smaller negative one near $z/h = 0.5$.

The sources of the negative vorticity associated with the larger flow cell can be seen in figure 18(b) where the variation of the vorticity equation terms as a function of the distance along a line parallel to the vertical axis at $z/h = 0.24$ is shown. Below the zero crossing of Ω at $y/h = 0.044$, the relative magnitudes of the various terms are as in figure 18(*a*). In the region where Ω is negative, large contributions to its production are made by the viscous and secondary stress term near the zero crossing of the vorticity, with the stress anisotropy term acting now as a sink. The former Reynolds stress term quickly turns into a sink of (negative) vorticity further from the wall. Near $y/h = 0.07$ the production of vorticity is dominated by viscous diffusion and mostly balanced by the anisotropy term. Near the corner bisector, $y/h = 0.24$, viscous effects are small, with approximately similar contributions to the production of negative vorticity being made by the convection and anisotropy term which are cancelled by the shear stress term. Further away from the vertical wall the various terms become numerically smaller with more complicated behaviour, figure 17. In general, the anisotropy and viscous terms tend to dominate the regions of positive and negative mean vorticity away from the corner bisector.

It appears from the above that the production of, in this case positive, mean vorticity within the formal viscous sublayer, coupled with the zero-Ω constraint on the bisector due to symmetry, is mainly responsible for the presence of mean vorticity in the bulk of the flow. This is consistent with the visual observation of the streamwise-averaged secondary flow field at different times of the simulation, which indicates that the flow near the sides of each corner and toward the wall bisectors is much more persistent than the flow cells themselves. Viscous diffusion plays a major part in the transport of mean vorticity whereas convection is weak by comparison. The secondary stress acts mainly as a sink term for the local vorticity.

The importance of the secondary stress term in the secondary flow modelling was identified by Demuren & Rodi, and the present results strongly support their assumption. However, the simulation results show that viscous effects are much greater than the mean convection whereas Demuren & Rodi assumed the reverse. It is noted that these observations are applicable to low-Reynolds-number flows, although the effects of increasing the Reynolds number may be only to push the various extrema further into the corner in terms of the global scales. If so, then the present results imply that robust modelling of the secondary flows will depend on finding suitable wall functions. The advantage of this approach would be that these functions are local and may be more easily approximated than the complicated behaviour of the various stresses over most of the flow field.

7. Conclusions

The fully developed turbulent flow through a straight duct of square cross-section was simulated using a centred finite-difference scheme. The Reynolds number based on the bulk velocity and hydraulic diameter was 4410 and the total number of grid points employed was 16.1×10^6. Lower-resolution runs were made to confirm the validity of the results presented herein. Owing to the long streamwise velocity scales found in early computations of this work, it was also necessary to confirm the convergence of the simulation results with respect to the streamwise length of the computational box. Turbulent statistics along the wall bisector of the duct were found to be in good agreement with plane channel flow data. Measurements in low-Reynolds-number square-duct flows and simulation results are in close agreement.

The mean secondary flow field of the simulated flow is in good qualitative agreement with higher-Reynolds-number experiments. In the low-Reynolds-number simulation, the maximum secondary velocity is about 2% of the bulk velocity but it is found near the corner walls rather than near the corner bisectors. Because the secondary velocities in the vicinity of the wall bisectors are a fraction of that maximum, the mean flow about the bisector is not quite symmetric in the statistics of the simulation. When the mean secondary flow field is averaged over all octants, an additional flow cell is found between the larger corner flow and the wall bisector. There is no direct experimental evidence for the existence of this flow feature and this is likely to remain so since the accuracy of present experimental techniques does not permit measuring such small velocities. However, the secondary flow field affects the distribution of the wall shear stress, which in the simulated flow shows a local maximum at each mid-wall point in addition those due to the larger flow cells near each corner. It is likely that the wall stress can be measurable but the use of the 'Clauser plot' method is not feasible because of both the high accuracy required and the uncertainty in the parameters of the logarithmic law.

If one excludes the region near the wall bisector where the smaller secondary flow cells are found, the mean streamwise vorticity field within an octant has two extrema of opposite sign. Assuming that the sign of the mean vorticity at the centre of the large flow cell is negative, then the vorticity has a minimum there. The vorticity along a line starting from this minimum towards the nearest wall increases monotonically to reach a positive maximum at the wall. It is interesting that the value of the wall maximum is more than twice the magnitude of the vorticity at the centre of the secondary flow cell. The Reynolds stress terms of the equation for this vorticity component, calculated from the simulation, attain their extrema in the viscous sublayer with substantial production of positive vorticity within the viscous sublayer. Viscous diffusion of the vorticity has been found to play a much more significant role than secondary convection. A theory on the flow structures that give rise to the observed mean flow is not yet available.

The author wishes to thank Professors I. L. Rhyming and M. Landahl, and Dr P. R. Voke for their help. Thanks are also due to Mr G. McGrath and Drs R. Cheesewright and D. G. Petty of the Queen Mary and Westfield College, London, for their timely experimental work. The project was part of an ERCOFTAC cooperative program. Computing resources were provided by the Service Informatique Central of Ecole Polytechnique Fédérale de Lausanne.

REFERENCES

Alfredsson, P. H., Johansson, A. V., Haritonidis, J. H. & Eckelmann, H. 1988 The fluctuating wall shear stress and the velocity field in the viscous sublayer. *Phys. Fluids* **31**, 1026–1033.

Bradshaw, P. 1987 Turbulent secondary flows. *Ann. Rev. Fluid Mech.* **19**, 53–74.

Chapman, D. R. & Kuhn, G. D. 1986 The limiting behaviour of turbulence near the wall. *J. Fluid Mech.* **170**, 265–292.

Cheesewright, R., McGrath, G. & Petty, D. G. 1990 LDA measurements of turbulent flow in a duct of square cross section at low Reynolds number. *Aeronautical Engineering Dept. Rep.* ER 1011. Queen May Westfield College, University of London.

Demuren, A. O. & Rodi, W. 1984 Calculation of turbulence-driven secondary motion in non-circular ducts. *J. Fluid Mech.* **140**, 189–222.

Jones, O. C. 1976 An improvement in the calculation of turbulent friction in rectangular ducts. *Trans. ASME* J: *J. Fluids Engng* **98**, 173–181.

Kim, J. & Moin, P. 1985 Application of a fractional-step method to incompressible Navier–Stokes equations. *J. Comput. Phys.* **59**, 308–323.

Kim, J., Moin, P. & Moser, R. 1987 Turbulent statistics in fully developed channel flow at low Reynolds number. *J. Fluid Mech.* **177**, 133–166.

KNIGHT, D. W. & PATEL, H. S. 1985 Boundary shear in smooth rectangular ducts. *J. Hydraul. Engng ASCE* **111**, 29–47.

KREPLIN, H. P. & ECKELMANN, H. 1979 Behavior of the three fluctuating velocity components in the wall region of a turbulent channel flow. *Phys. Fluids* **22**, 1233–1239.

LEUTHEUSSER, B. E. 1963 Turbulent flow in rectangular ducts. *J. Hydraul. Div., ASCE* **89**, 1–19.

LUND, E. G. 1977 Mean flow and turbulence characteristics in the near corner region of a square duct. M.S. thesis, University of Washington.

MORTON, B. R. 1984 The generation and decay of vorticity. *Geophys. Astrophys. Fluid Dyn.* **28**, 277–308.

NEZU, I., NAKAGAWA, H. & TOMINAGA, A. 1985 Secondary currents in a straight channel flow and the relation to its aspect ratio. In *Turbulent Shear Flows 4* (ed. L. J. S. Bradbury *et al.*) pp. 246–260. Springer.

NIEDERSCHULTE, M. A. 1989 Turbulent flow through a rectangular channel. Ph.D. thesis, University of Illinois at Urbana-Champaign.

NISHINO, K. & KASAGI, N. 1989 Turbulence statistics measurement in a two-dimensional channel flow using a three-dimensional particle tracking velocimeter. In *Seventh Symp. on Turbulent Shear Flows, Stanford University, August 21–23.*

POPOVICH, A. T. & HUMMEL, R. L. 1967 Experimental study of the viscous sublayer in turbulent pipe flow. *AIChE J.* **13**, 854–860.

SCHLICHTING, H. 1979 *Boundary-Layer Theory.* McGraw-Hill.

SCHUMANN, U. 1975 Subgrid scale model for finite difference simulations of turbulent flows in plane channels and annuli. *J. Comput. Phys.* **18**, 376–401.

SPEZIALE, G. C. 1986 The dissipation rate correlation and turbulent secondary flows in noncircular ducts. *Trans. ASME* J: *J. Fluids Engng.* **108**, 118–120.

SWARZTRAUBER, P. N. 1974 A direct method for the discrete solution of separable elliptic equations. *SIAM J. Numer. Anal.* **11**, 1136–1150.

TEITEL, M. & ANTONIA, R. A. 1990 The interaction region of a turbulent duct flow. *Phys. Fluids* A **2**, 808–813.

TOWNSEND, A. A. 1976 *The Structure of Turbulent Shear Flow.* Cambridge University Press.

WEI, T. & WILLMARTH, W. W. 1989 Reynolds-number effects on the structure of a turbulent channel flow. *J. Fluid Mech.* **204**, 57–95.

YONG, C. K. 1988 Zur Wirkung von Polymer-Additiven auf die kohärente Struktur turbulenter Kanalströmungen. Doctoral dissertation, University of Essen.